



Enhanced interfacial effect-induced asymmetric coupling boost electroreduction of CO₂ to ethylene

Yong Zhang^a, FeiFei Chen^a, Xiaoya Hao^a, Yingda Liu^a, Wentao Wu^a, Xinghua Zhang^b, Zehao Zang^b, Hong Dong^a, Weihua Wang^a, Feng Lu^a, Zunming Lu^b, Hui Liu^{c,*}, Hui Liu^{a,*}, Feng Luo^d, Yahui Cheng^{a,*}

^a Department of Electronic Science and Engineering and Tianjin Key Laboratory of Process Control and Green Technology for Pharmaceutical Industry, Nankai University, Tianjin 300350, China

^b School of Material Science and Engineering, Hebei University of Technology, Tianjin 300130, China

^c Research Group of Quantum-Dot Materials & Devices, Institute of New-Energy Materials, Tianjin University, Tianjin 300350, China

^d Tianjin Key Lab for Rare Earth Materials and Applications, Center for Rare Earth and Inorganic Functional Materials, School of Materials Science and Engineering, Nankai University, Tianjin 300350, China

ARTICLE INFO

Keywords:

CO₂ electroreduction

Ethylene

Cu/Ag bimetallic catalysts

Interfacial effect

Asymmetric C-C coupling

ABSTRACT

Electroreduction of CO₂ to C₂H₄ is a promising strategy for carbon neutralization. However, the kinetic challenge of *CO dimerization, particularly at high current-density, limits its suitability for industrial production. Here, we report that Cu/Ag bimetallic catalyst (Cu₅₂Ag₄₈) with strong interfacial effect can promote high C₂H₄ selectivity at high current-density. We find that the elaborately designed Cu/Ag interface not only inhibits HER and ethanol formation by weakening H adsorption, but also promotes the formation of *CHO intermediates, achieving an unusual asymmetric *CO-*CHO coupling instead of the common symmetric *CO-*CO coupling. Subsequently, the Faradaic efficiency of C₂H₄ over Cu₅₂Ag₄₈ is significantly increased to 69.2% at a high current-density of up to 450 mA cm⁻². The interfacial effect-induced *CO-*CHO coupling can be extended to other metals with weak H and O adsorption such as Cu/Zn and Cu/Au, thereby boosting the production of C₂H₄ in CO₂RR.

1. Introduction

Electrochemical carbon dioxide (CO₂) reduction reaction (CO₂RR) powered by renewable electricity is a promising approach to convert CO₂ into fuels and chemical feedstocks, helping promote carbon neutrality [1–3]. The production of multi-carbon (C₂₊) products such as ethylene (C₂H₄) and ethanol (EtOH) by CO₂RR is highly attractive because of their high energy density and important economic value [4]. Among the major C₂₊ products, C₂H₄ has been prioritized as a target in CO₂RR as it is a crucial building block molecule with high demand and limited sources [5–7]. Copper (Cu)-based catalysts have been extensively studied and optimized to improve CO₂ to C₂H₄ conversion, because they are the only monometal surface with decent selectivities for C₂₊ products [8–10]. Despite recent progress in the electrochemical CO₂RR to C₂H₄ [11–14], the reaction is still falls below the requirement of industrial relevant current-density and selectivity due to the sluggish kinetics of carbon-carbon (C-C) coupling reaction.

For CO₂RR to C₂H₄ at high current-density, C-C coupling is believed to be the key reaction step that determines the activity and selectivity [2, 9]. Adsorbed CO (*CO) dimerization is considered as the main C-C coupling mechanism for C₂H₄ production [6,10,13]. However, the kinetic barrier of *CO dimerization on the Cu surface increases with negative potential, resulting in the closure of the C₂H₄ generation pathway at intermediate potential [15,16]. Therefore, the selective formation of C₂₊ products at high current-density still confronts huge challenges in consideration of the kinetic difficulty of *CO dimerization at high potential. Recently, many studies suggest that the protonation of *CO to *CHO prior to C-C coupling is kinetically and thermodynamically favorable at high potential or under acidic to neutral pH [15–20]. In particular, the asymmetric *CO-*CHO coupling involving *CHO is a favorable downhill reaction, which is beneficial for CO₂RR to C₂H₄ under high current-density and even acidic conditions [15–18]. Nevertheless, despite having reported some fancy Cu-based catalysts, the production of C₂H₄ using asymmetric *CO-*CHO coupling mechanism

* Corresponding authors.

E-mail addresses: hui_liu@tju.edu.cn (H. Liu), liuhui@nankai.edu.cn (H. Liu), chengyahui@nankai.edu.cn (Y. Cheng).

<https://doi.org/10.1016/j.apcatb.2023.123666>

Received 26 October 2023; Received in revised form 19 December 2023; Accepted 24 December 2023

Available online 25 December 2023

0926-3373/© 2023 Elsevier B.V. All rights reserved.

under high current-density remains limited. Instead, due to the overwhelming coverage of *CO or *CHO intermediates on these catalysts, they always exhibit symmetric *CO - *CO coupling or *CHO - *CHO coupling under high current-density [2,9,13,20]. Therefore, it is urgently desirable to develop a meticulously designed catalyst structure to balance the coverage of *CO and *CHO on the catalyst surface to achieve *CO - *CHO coupling.

In terms of *CHO generation, strategies including dopant and modification engineering [20], oxide-derived catalysis [7], polymer catalysis [21] and interfacial regulation [22–24] have been proposed to improve the hydrogenation of *CO to *CHO . Among these strategies, interfacial regulation is attractive because the interfacial effect is usually effective for specific reactions and the interface components can be freely controlled. In a series of recent works, researchers constructed metal/compound interfaces such as $Cu/Ce(OH)_x$, Cu/Cu_2O , $Cu/CuAl_2O_4/CuO$, and Cu/C_3N_4 , which usually accelerate H_2O dissociation and enhance H adsorption, thus promoting the formation of *CHO [7, 22–24]. However, the activated *H can lead to enhanced competitive hydrogen evolution reaction (HER) and increase the selectivity of EtOH in post C-C coupling steps [22,23,25]. Therefore, these catalysts exhibit high selectivity for H_2 or EtOH in CO_2RR , which is obviously unfavorable for the generation of C_2H_4 . In this work, we aim to design and optimize Cu interface structures to promote C_2H_4 generation at high current-density by utilizing *CO - *CHO coupling. To achieve this goal, we focus on maintaining sufficient supply of *CO and facilitating its hydrogenation to *CHO while reducing H adsorption to limit HER and EtOH formation. Hence, we simultaneously consider two key aspects in interfacial design: (1) increasing the proportion of interfaces in the overall catalyst to enhance the interfacial effect and promote the formation of *CHO ; (2) introducing metals that have weak H and O adsorption (e.g., Ag, Zn and Au) to form interfaces with Cu [8]. The introduction of such Cu/metal interfaces not only enhances the tandem effect [13,26–28], ensuring sufficient coverage of *CO , but also weakens binding of *H compared to *CO on the catalyst surface, suppressing HER and the selectivity of EtOH in C_{2+} products.

Herein, we report Cu/Ag bimetallic catalysts with abundant Cu/Ag interfaces, which are stable under CO_2RR conditions and catalyze the conversion of CO_2 to C_2H_4 with high Faradaic efficiency (FE) at industry-relevant current densities. The Cu/Ag bimetallic catalysts are obtained using magnetron sputtering technology combined with a unique catalyst deposition process to ensure high Cu/Ag interface ratio. During the deposition, sequentially change the target material to alternately grow Cu and Ag with a special thin layer structure. As a result, the CO_2RR tests of the acquired $Cu_{52}Ag_{48}$ delivered an $FE_{C_2H_4}$ of 69.2% and a total C_{2+} FE of 81.2% at a high current-density of 450 mA cm^{-2} in a membrane electrode assembly (MEA) system. Moreover, $Cu_{52}Ag_{48}$ exhibits a high single-pass carbon efficiency of 21.8% to C_2H_4 and stable electrolysis for 32 h at 275 mA cm^{-2} using acidic electrolyte. Density functional theory (DFT) calculations and in-situ Raman spectra suggest that the Cu/Ag interface facilitate the formation of *CHO intermediate, and the asymmetric *CO - *CHO coupling is energetically more favorable than the symmetric coupling at the Cu/Ag interface, which improves the selectivity of C_2H_4 . This interfacial regulation can also be extended to the interface of Cu with other weakly H and O adsorbed metals, such as Cu/Zn interface and Cu/Au interface, to promote the reduction of CO_2 to C_2H_4 .

2. Experimental

2.1. Preparation of the catalysts

Cu/Ag bimetallic catalysts were deposited on the Gas diffusion electrode (YLS-30 T, Fuel Cell Store) by alternating magnetron sputtering of Cu and Ag targets (99.99%, Hebei JiuYue Advanced Material Technology). The chamber pressure was vacuumized to 10^{-7} Torr by the molecular pump, and then injected Ar gas to keep the pressure at $6 \times$

10^{-3} Torr and the Gas diffusion electrode (GDE) was kept rotating at a slow speed of 20 rpm during deposition. Cu and Ag were deposited at rates of approximately 0.35 Å s^{-1} and 0.70 Å s^{-1} , respectively. In order to increase the Cu/Ag interface, firstly deposited 60 s thin Cu layer on GDE, then deposited thin Ag layers for 30 s, 50 s, 70 s and 90 s respectively to obtain different Cu-Ag ratios, and finally deposited a thin Cu layer for 60 s. The Cu/Ag atomic ratio was measured by inductively coupled plasma mass spectrometry (ICP-MS), and the Cu/Ag catalysts were named as $Cu_{70}Ag_{30}$, $Cu_{58}Ag_{42}$, $Cu_{52}Ag_{48}$ and $Cu_{42}Ag_{58}$ respectively according to the Cu/Ag atomic ratio. By extending the deposition time, thicker $Cu_{52}Ag_{48}$ was prepared for comparison, with the thickness of 40 nm ($Cu_{300\text{ s}}Ag_{350\text{ s}}Cu_{300\text{ s}}$) and 100 nm ($Cu_{720\text{ s}}Ag_{840\text{ s}}Cu_{720\text{ s}}$), and were named as $Cu_{52}Ag_{48}$ -40 nm and $Cu_{52}Ag_{48}$ -200 nm, respectively. Cu/Zn and Cu/Au bimetallic catalysts were prepared using a similar procedure as Cu/Ag bimetallic catalysts, with the only variation being the sputtering times for Zn and Au, which were 120 s and 200 s, respectively.

2.2. Electrochemical CO_2RR measurements

The details of Electrochemical CO_2RR methods are shown in the [Supplementary Materials](#).

2.3. Materials characterization

X-ray diffraction (XRD) patterns were obtained on a powder diffractometer (Rigaku Smart Lab 3 kW) using Cu K_α X-ray source and the catalysts were deposited on the FTO. Scanning electron microscopy (SEM) images of the samples were obtained using a JSM-7800 F scanning electron microscopy. Transmission electron microscopy (TEM) and high resolution TEM (HRTEM) images were obtained with a Talos F200X G2 transmission scanning microscopy at 200 kV. X-ray photoelectron spectroscopy (XPS) was performed on a ThermoFisher ESCA-LAB 250Xi instrument using a Mg K_α X-ray source. For XPS testing of thicker samples, the sample was scraped off the GDE, after ultrasonic crushing, the powder is pressed for testing. The binding energy of the collected spectra was calibrated by the C 1 s binding energy of 284.6 eV. Centre of gravity calculation for the valence band spectra is conducted as $\frac{\int N(\epsilon) \epsilon d\epsilon}{\int N(\epsilon) d\epsilon}$ in the range of $0 \sim -9.0\text{ eV}$, where $N(\epsilon)$ is the density of states. ICP-MS data were determined using an Agilent 7850 (Ms) system. The gas products were quantified by gas chromatography (GC, FULL INSTRUMENTS GC9790 Plus) and the liquid product was detected by liquid nuclear magnetic resonance spectroscopy (Bruker, AVANCE III 400 MHz NanoBAY). The contact angle was measured by the sessile drop method using JC2000C1 contact angle system at room temperature.

In-situ Raman spectra was recorded on a laser Raman spectrometer (LabRAM HR Evolution) with 785 nm laser with 25% intensity. The catalysts were deposited on the GDE whereas the backside and edges of the GDE were covered with epoxy to prevent the parasitic hydrogen evolution reaction. The electrochemical CO_2RR was performed in a home-made Raman cell with a quartz optical window, a Ag/AgCl (3.0 M KCl) reference electrode and a Pt counter electrode. The Raman cell was filled with 0.1 M CO_2 -saturated $KHCO_3$ electrolyte, and the CO_2 flow rate was maintained at 5 sccm. During the measurement, each potential lasted for 5 min and then each Raman spectroscopy was recorded with three accumulations with an acquisition time of 20 s

2.4. DFT calculation

DFT calculations were performed in the Vienna ab initio simulation package (VASP). The details of calculation methodology are shown in the [Supplementary Materials](#).

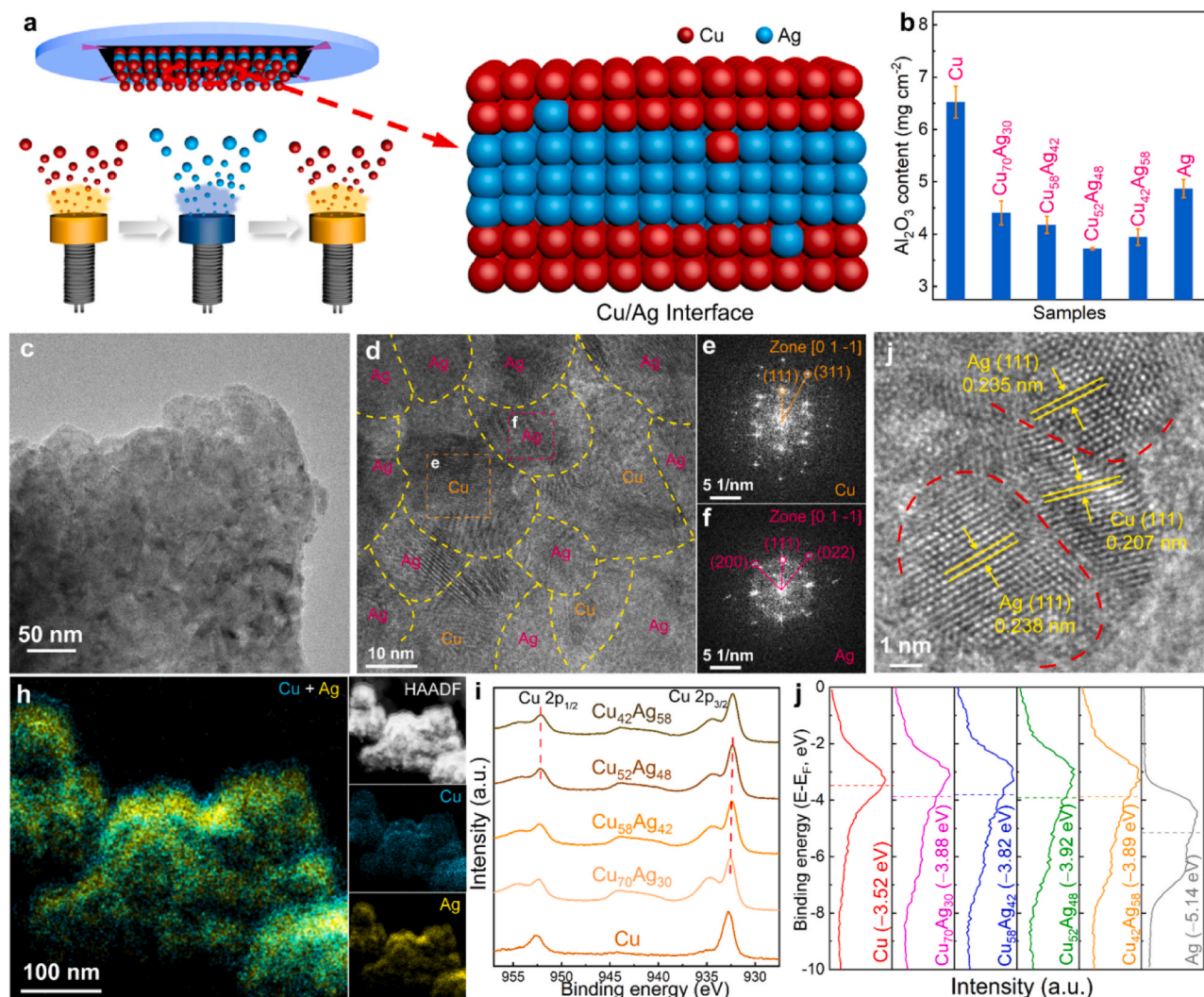


Fig. 1. (a) Schematic illustration of the synthesis of Cu/Ag catalysts by magnetron sputtering. (b) The amount of Al₂O₃ in Cu, Cu/Ag catalysts and Ag, respectively. (c) TEM and (d) HRTEM images of Cu₅₂Ag₄₈. FFT patterns of the selected (e) Cu domain and (f) Ag domain. (g) Enlarged HRTEM image of Cu₅₂Ag₄₈. (h) High-angle annular dark-field scanning TEM (HAADF-STEM) image and EDS elemental mapping of Cu₅₂Ag₄₈. XPS spectra of (i) Cu 2p and (j) surface valence band of Cu, Cu/Ag catalysts and Ag, respectively.

3. Results and discussion

3.1. Synthesis and structural characterizations of Cu/Ag catalysts

The Cu/Ag bimetallic catalysts were prepared by sequentially depositing thin layers of Cu and Ag on the GDE, while controlling the time of sputtering Ag to obtain different Cu/Ag atomic ratios (Fig. 1a). The Cu/Ag atomic ratio and film thickness was determined using ICP-MS. The Cu/Ag catalysts are then named based on their respective Cu/Ag atomic ratios (Table S1), and are referred to as Cu₇₀Ag₃₀, Cu₅₈Ag₄₂, Cu₅₂Ag₄₈ and Cu₄₂Ag₅₈. SEM images and energy-dispersive X-ray spectroscopy (EDS) (Figs. S1 and S2) elemental mapping reveal that the Cu/Ag catalysts cover the GDE and preserve the nanoparticles morphology of the GDE substrate. To assist in determining the maximal proportion of Cu/Ag interface in different Cu/Ag catalysts, we performed selective atomic layer deposition (ALD) of Al₂O₃ on catalysts as an auxiliary (Experimental Methods in Supplementary Materials) [29], as DFT calculations showed that Al₂O₃ is more inclined to selectively grow on pure Cu surface rather than Cu/Ag interface (Fig. S3). ICP analysis presents significant variations in the content of Al₂O₃ among different samples (Fig. 1b), that is, the content of Al₂O₃ on pure Cu (6.52 mg cm⁻²) and pure Ag (4.87 mg cm⁻²) is higher than that on

Cu/Ag catalysts, and Cu₅₂Ag₄₈ exhibits the lowest Al₂O₃ content of 3.72 mg cm⁻², indicating that Cu₅₂Ag₄₈ has the largest interfacial proportion among Cu/Ag catalysts with various Cu/Ag ratios.

XRD pattern reveals that the Cu and Ag domains remain separated from each other and no alloy structure is formed (Fig. S4). TEM image (Fig. 1c) of Cu₅₂Ag₄₈ exhibits that the Cu and Ag phase come into contact with each other to form a homogeneous film, rather than small and separate nanoparticles. In the HRTEM image of Cu₅₂Ag₄₈ (Fig. 1d), numerous Cu and Ag domains are observed with clearly defined interfacial connections, which is highlighted by the yellow dashed line. The plane spacing in zone (01 $\bar{1}$) derived from the selected-area fast Fourier transform (FFT) spots (Fig. 1e) are 0.21 nm and 0.11 nm, which are indexed as Cu (111) and Cu (311), respectively. The FFT spots (Fig. 1f) of Ag domain match well with Ag (111), Ag (200) and Ag (022), respectively. In addition, the HRTEM image (Fig. 1g) of Cu₅₂Ag₄₈ shows an interface structure formed by two Ag domains and one Cu domain with a width as narrow as 3 nm, indicating that the Cu/Ag interfaces are abundant in the Cu/Ag catalysts. In reference to previous report [30], a simple geometric model was employed to characterize the interface density on the catalysts surfaces (Table S2). The interface density is $265.2 \pm 10.6 \mu\text{m}^{-1}$ for Cu₅₂Ag₄₈, which is 4 to 20 times higher than that of other interface catalysts. Hence, the abundant interface density is the

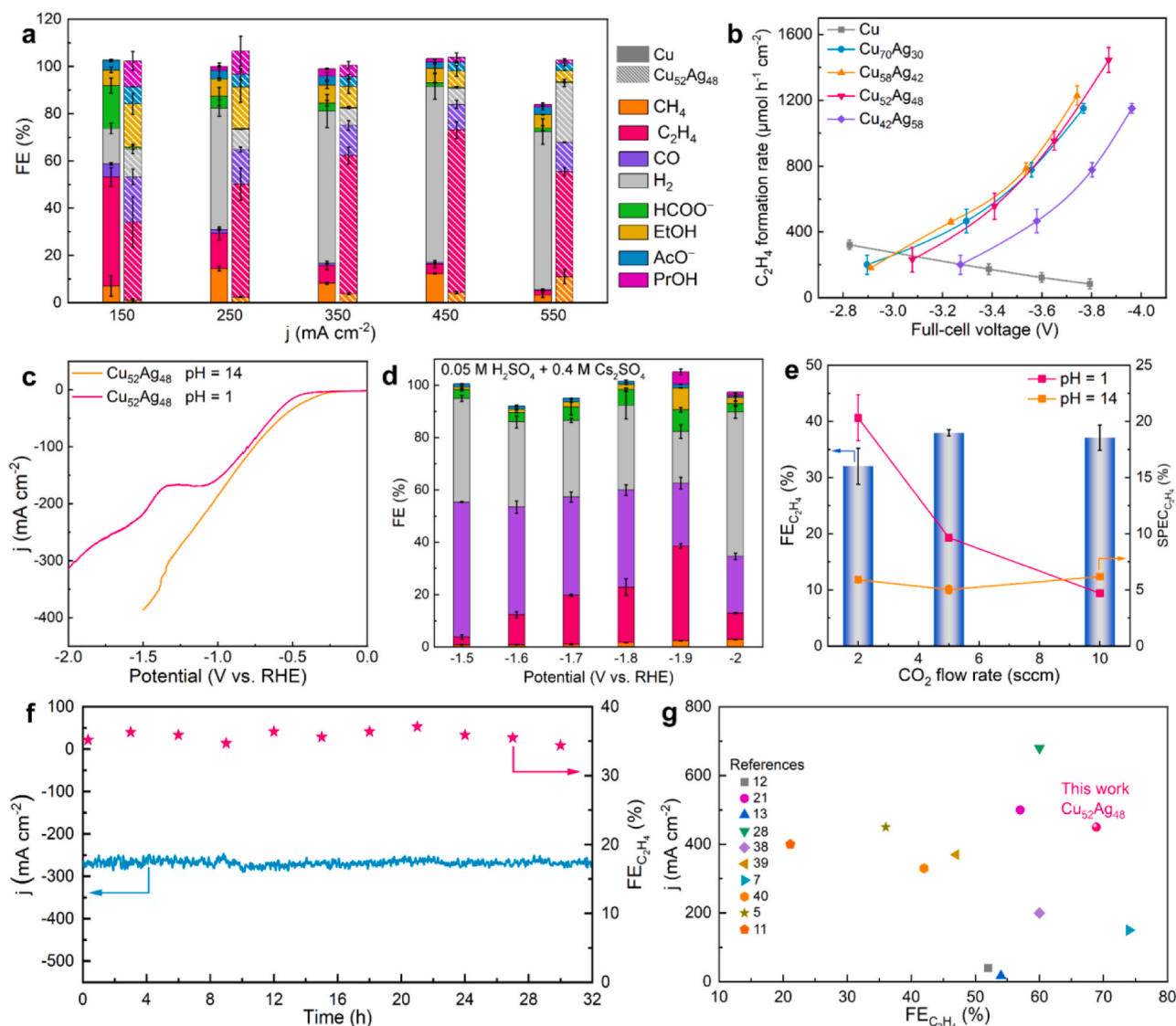


Fig. 2. (a) FEs of major CO₂RR products obtained on Cu and Cu₅₂Ag₄₈. (b) The formation rates of C₂H₄ under different applied cell voltages over Cu and Cu/Ag catalysts. (c) LSV curves of Cu₅₂Ag₄₈ at the alkaline electrolyte and acidic electrolyte. (d) FEs of major CO₂RR over Cu₅₂Ag₄₈ in the flow cell with acidic electrolyte. (e) FEs of Cu₅₂Ag₄₈ in the acidic electrolyte and SPEC_{C₂H₄} of Cu₅₂Ag₄₈ at different CO₂ flow rates (applied current, 500 mA). (f) Long-term stability of CO₂RR at -1.9 V for Cu₅₂Ag₄₈. (g) A comparison of some top Cu-based catalysts reported so far. Error bars in these fig. correspond to the standard deviation of two or three independent measurements.

key feature that sets Cu₅₂Ag₄₈ apart from other Cu/Ag interface catalysts [13,26]. HRTEM images of Cu₇₀Ag₃₀, Cu₅₈Ag₄₂ and Cu₄₂Ag₅₈ also show that the atomic arrangements of Cu and Ag domains cross each other at the interfaces (Fig. S5). Further EDS elemental mapping analysis reveals a clear interfacial connection between Cu and Ag (Fig. 1h, S6 and S7), and the Cu/Ag elemental distribution is consistent with the Cu/Ag interface formed by layered sputtering.

XPS was used to analyze the surface state of the Cu/Ag catalysts. The Cu 2p peaks of Cu₇₀Ag₃₀, Cu₅₈Ag₄₂ and Cu₅₂Ag₄₈ (Fig. 1i) gradually shift to lower binding energy as the atomic ratios of Ag increase, suggesting the existence of electron transfer from Ag to Cu via the Cu/Ag interface [13,31]. The Ag 3d XPS peaks of Cu/Ag catalysts moving towards higher binding energy (Fig. S8a) further confirms the electron transfer from Ag to Cu. It is worth noting that the Ag 3d XPS, Cu 2p XPS and Cu LMM Auger peaks (Fig. S8b) of Cu₄₂Ag₅₈ do not shift compared with that of Cu₅₂Ag₄₈, indicating that their electron transfer between the interface no longer increases with the increase of Ag content. This illustrates that the Cu/Ag interface has reached its maximum in Cu₅₂Ag₄₈. The XPS surface valence band spectra (Fig. 1j) reveals that the d-band and its

gravity of the Cu/Ag catalysts is slightly shifted away from the Fermi level compared with that of pure Cu, signifying a slightly decrease in the binding strength to the intermediates [32].

3.2. CO₂RR performance

The CO₂RR performance of pure Cu and four kinds of Cu/Ag catalysts were firstly tested in a MEA system using 1.0 M KOH as the electrolyte (Fig. S9). The major gas products CH₄, C₂H₄, CO and H₂ were quantified by gas chromatographic (GC), and the major liquid products HCOO⁻, acetate (AcO⁻), EtOH and propanol (PrOH) were quantified by ¹H NMR (Figs. S10 and S11). The linear sweep voltammetry (LSV) curves of Cu and Cu/Ag catalysts are shown in Fig. S12 and the current densities follow the order of Cu₄₂Ag₅₈ < Cu₅₂Ag₄₈ < Cu₅₈Ag₄₂ < Cu₇₀Ag₃₀ < Cu. The FEs were calculated for both gas and liquid products at applied current densities ranging from 150 mA cm⁻² to 550 mA cm⁻². Compared with Cu, the Cu/Ag catalysts all exhibit higher FE for C₂H₄ (FE_{C₂H₄}) at high current densities, especially, exceeding 50.0% at 450 mA cm⁻² (Fig. 2a and S13). Among the four Cu/Ag catalysts,

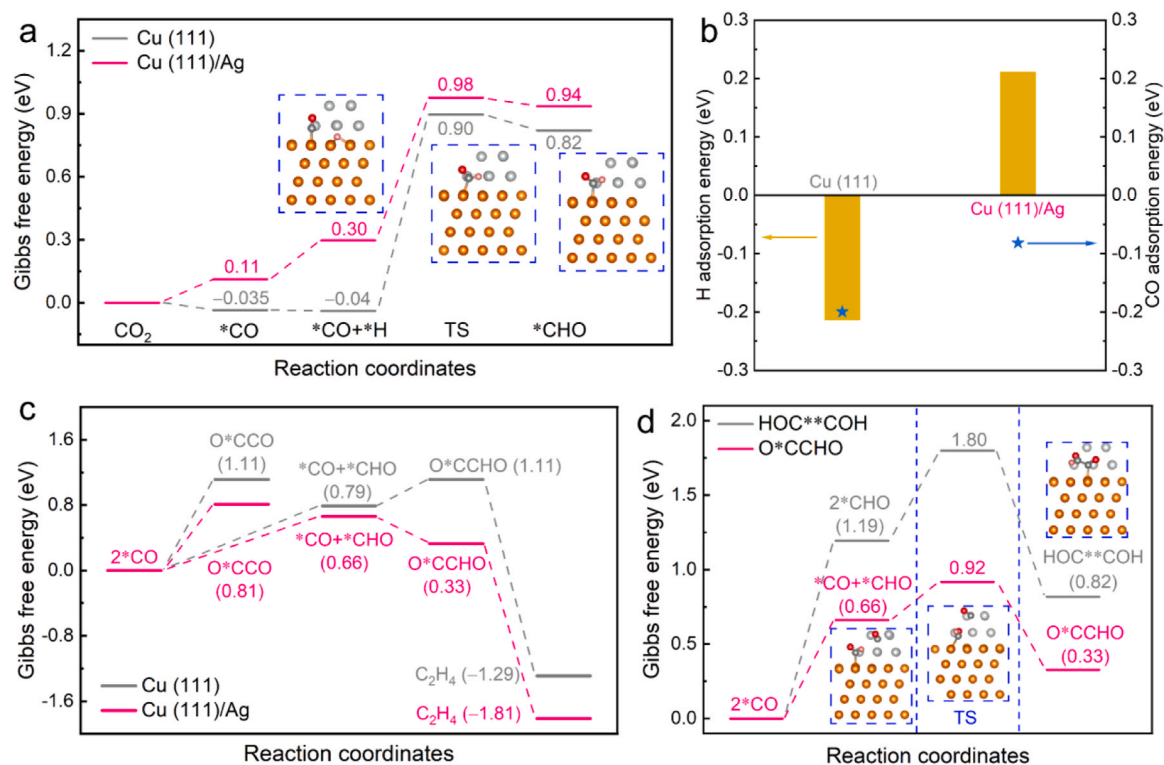


Fig. 3. (a) Gibbs free energy diagram of CO₂RR to *CO and hydrogenation of *CO on Cu (111) and Cu (111)/Ag. Inset fig. are side-view geometries of intermediate (*CO+*H, TS_{CHO} and *CHO) on Cu (111)/Ag. (b) The H and CO adsorption energies on Cu (111) and Cu (111)/Ag. (c) Gibbs free energy diagram of *CO-*CO and *CO-*CHO coupling on Cu (111) and Cu (111)/Ag. (d) Gibbs free energy diagram of *CO-*CHO coupling and *CHO-*CHO coupling on Cu (111)/Ag. Inset fig. are side-view geometries of intermediate (*CO+*CHO, TS_{O*CCO} and O*CCHO) on Cu (111)/Ag. Cu, brown; Ag, white; C, gray; O, red and H, pink.

Cu₅₂Ag₄₈ exhibits the highest FE_{C₂H₄} of 69.2% at 450 mA cm⁻² (Fig. S14). In contrast, the FE_{C₂H₄} of Cu is only 4.0%. Notably, the total FE_{C₂+} for Cu₅₂Ag₄₈ is up to 81.2% at the current-density of 450 mA cm⁻². Moreover, Cu₅₂Ag₄₈ exhibits high C₂H₄ selectivity at high current-density (450 mA cm⁻²), with a FE_{C₂H₄}/FE_{EtOH} ratio of 9.97 (Fig. S15), significantly higher than that of 1.79 at low current-density (150 mA cm⁻²). The electrochemical active surface area (ECSA) normalized FE_{C₂H₄} (obtained through the double-layer capacitance method) on Cu₅₂Ag₄₈ is larger than those of the other Cu/Ag catalysts (Figs. S16 and S17), confirming the highest intrinsic activity of Cu₅₂Ag₄₈ due to the most Cu/Ag interface. The formation rates of C₂H₄ over Cu/Ag catalysts (Fig. 2b) increase with increasing applied potentials, while the opposite trend is observed for Cu. The C₂H₄ formation rates of Cu₅₂Ag₄₈ reaches the maximum of 1445.07 μmol h⁻¹ cm⁻² and a C₂H₄ half-cell energy efficiency of 20.9% with current-density of 450 mA cm⁻² at 3.87 V full-cell voltage.

Although the alkaline MEA is very effective for the electrochemical CO₂RR, long-term stability remains challenging due to salt accumulation and flooding of GDE (Fig. S18) [33]. The stability test of Cu₅₂Ag₄₈ was conducted at a constant current of 350 mA cm⁻², with washing GDE performed every 2 h to overcome the loss of hydrophobicity and the salt accumulation. Over a period of 2 h, the FE_{C₂H₄} decreases from the initial value of 58.2% to 52.3%, and after washing the GDE, both the FE_{C₂H₄} and cell voltage return to their original state (Fig. S19). Unfortunately, the catalyst completely loses its activity after 15 h. To improve the long-term stability and single-pass carbon efficiency (SPCE), CO₂ electrolysis was performed in a flow cell under acidic conditions (Fig. S20) [34–37]. Cu₅₂Ag₄₈ with the best performance in MEA was selected as the catalyst, and a layer of Nafion was coated on its surface to prevent corrosion under acidic conditions. In an alkaline flow cell (1.0 M KOH as electrolyte), Nafion coated Cu₅₂Ag₄₈ exhibits the similar performance as MEA system (Fig. S21). Based on previous reports [34–36], 0.05 M H₂SO₄ + 0.4 M Cs₂SO₄ was selected as the electrolyte because

alkali cations can promote the formation of local neutral environments, which effectively inhibit the HER in acid conditions. The LSV curve of Cu₅₂Ag₄₈ displays a current-limiting plateau in 0.8 M Cs⁺ solution (Fig. 2c), revealing that the addition of Cs⁺ effectively suppressed the HER at potentials ranging from -1.1 V to more negative values [34]. Fig. 2d shows the performance of Cu₅₂Ag₄₈ in acidic electrolyte. CO and C₂H₄ are the major products of CO₂RR and the maximum FE_{C₂H₄} and partial current-density are 36.2% and 104.2 mA cm⁻² at -1.9 V, respectively. By progressively reducing the flow rate of CO₂ from 10 sccm to 2 sccm, the SPCE of the C₂H₄ product increases to a maximum of 21.8% at the current of 500 mA (Fig. 2e). Notably, Cu₅₂Ag₄₈ maintains a stable current-density (275 mA cm⁻²) and FE_{C₂H₄} (34.4%) during continuous CO₂RR operation in strong acid (Fig. 2f) for more than 32 h, which far exceeds the results under alkaline conditions. The contact angle test demonstrates that the hydrophobicity of the GDE does not decrease during long-term electrolysis (Fig. S22). ICP analysis indicates that Cu₅₂Ag₄₈ is only slightly corroded in the acidic electrolyte (Table S3). SEM images, HRTEM image and EDS elemental mapping of Cu₅₂Ag₄₈ show that morphology and Cu/Ag interface structure are maintained following the stability test (Figs. S23 and S24). In summary, Cu/Ag catalysts exhibit high activity for CO₂RR to C₂H₄ under both alkaline and acidic conditions, which is also confirmed by comparison with the reported Cu-based catalysts (Fig. 2g and Table S4) [5,7,11–13, 21,28,38–40]. It is apparent that the Cu₅₂Ag₄₈ exhibits higher FE_{C₂H₄} and current-density amongst these top catalysts.

3.3. Mechanism analysis

To further gain mechanistic insights into the CO₂RR active sites and reaction pathway of Cu/Ag catalysts, DFT calculations were performed on Cu (111) and Cu (111)/Ag (Experimental Methods in Supplementary Materials and the size effect of Ag slab is discussed in Fig. S25). The Cu/Ag interface was modeled by distributing a Ag₈ cluster on the surface of

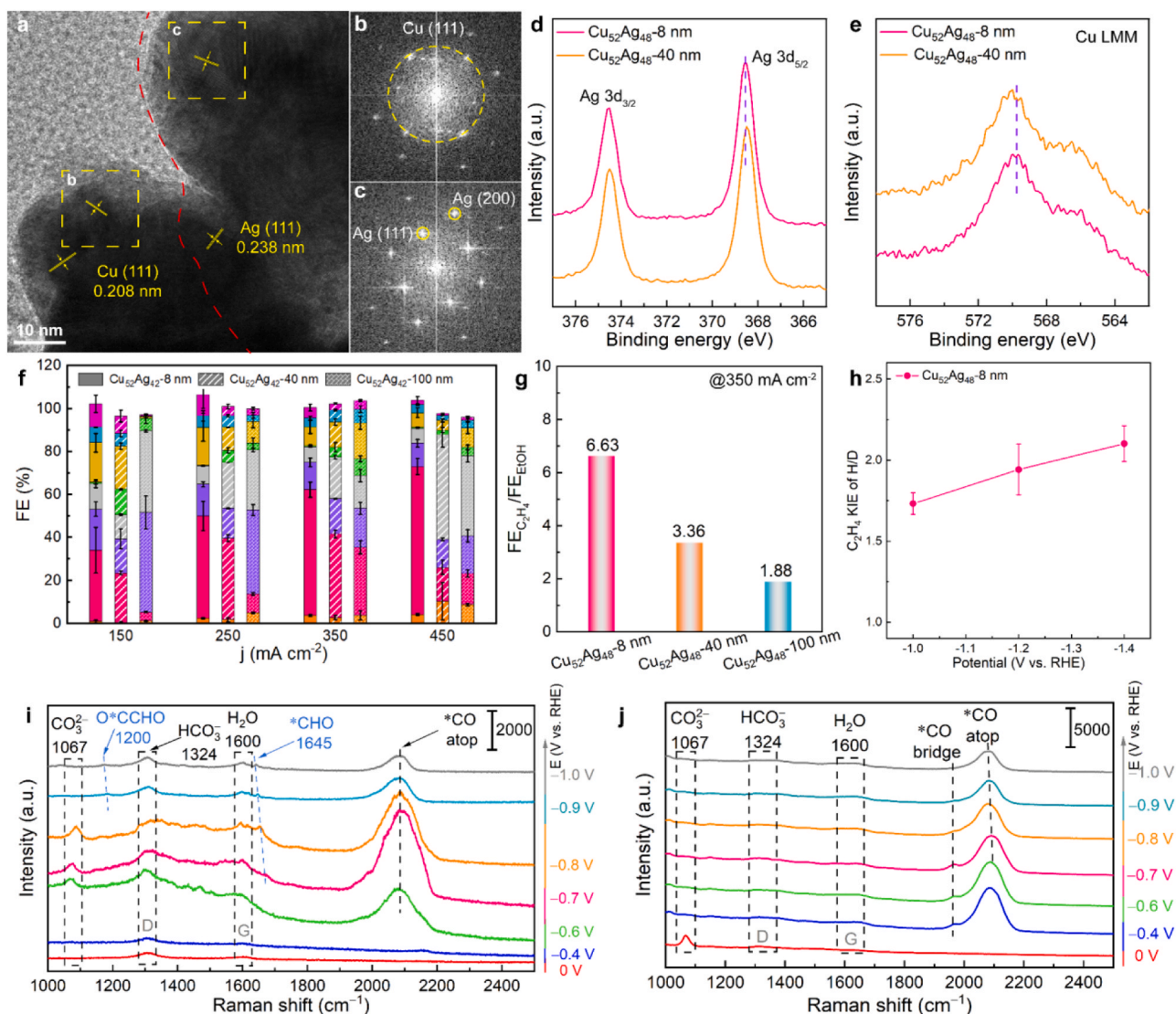


Fig. 4. (a) HRTEM image of Cu₅₂Ag₄₈-40 nm. FFT patterns of the selected (b) Cu domain and (c) Ag domain. (d) Ag 3d XPS spectra and (e) Cu LMM Auger for Cu₅₂Ag₄₈-8 nm and Cu₅₂Ag₄₈-40 nm. (f) FEs of major CO₂RR products and (g) FE_{C₂H₄}/FE_{EtOH} values at 350 mA cm⁻² obtained on Cu₅₂Ag₄₈-8 nm, Cu₅₂Ag₄₈-40 nm and Cu₅₂Ag₄₈-100 nm. (h) KIE of H/D in CO₂RR on Cu₅₂Ag₄₈-8 nm under the potential range from -1.0 V to -1.4 V. In-situ Raman spectra of (i) Cu₅₂Ag₄₈-8 nm and (j) Cu₅₂Ag₄₈-40 nm at the applied potential of 0 V to -1.0 V under CO₂RR.

Cu (111) [7,41]. The energy barriers of *CO hydrogenation and several possible C-C coupling paths were calculated to determine the preferred coupling path on both Cu and Cu/Ag interface structures (Figs. S26 and S27) [7,16,24].

Firstly, DFT calculations confirm that CO₂ can be easily converted to adsorbed CO (*CO) on both Cu (111) and Cu (111)/Ag (Fig. 3a). Subsequently, the energy barrier for the initial hydrogenation step (*CO to *CHO) decreases from 0.94 eV over Cu (111) to 0.68 eV over Cu (111)/Ag interface (Fig. 3a), indicating faster *CO hydrogenation rates at the Cu (111)/Ag interface. Due to the reaction energy required for *CHO formation is lower than that for *COH (1.35 eV), *CHO should be the major species formed from *CO hydrogenation on both surfaces (Fig. S28). To explore the reason for the accelerated *CO hydrogenation at the Cu/Ag interface, water dissociation calculations were further conducted (Fig. S29). The reaction energy for water dissociation at the Cu (111)/Ag (0.61 eV) is higher than that (-0.08 eV) at the Cu (111) surface. This suggests that the accelerated *CO hydrogenation at the Cu/Ag interface does not originate from sufficient *H coverage, which aligns with the lower FE of H₂ observed in experiments using the Cu/Ag catalysts. Density of states (DOS) (Fig. S30) reveal that the d-band center of

Cu (111)/Ag is located farther from the Fermi level compared to Cu (111), which indicates that the adsorption of intermediates on the Cu/Ag interface is weaker. In addition, since Ag is a metal with weak H and O adsorption, the adsorption of H on the Cu/Ag interface is much weaker than that of C-containing intermediates (such as CO). Specifically, compared with the situation on Cu surface, the adsorption energy of H on Cu(111)/Ag surface (0.21 eV) increases by 0.42 eV, while that of CO on Cu(111)/Ag surface only increases by 0.1 eV (Fig. 3b). Previous reports have indicated that the decrease in H adsorption and coverage can reduce the selectivity of EtOH [22,23,25], leading to an increase in the selectivity of C₂H₄ in the C₂₊ product. The differential charge density analysis (Fig. S31) further reveals that the electron interaction between *H and the substrate is weaker on Cu (111)/Ag, which will facilitate *H migration and subsequent addition to the C atoms of *CO, ultimately leading to the formation of *CHO.

The traditional consensus regarding the C-C coupling mechanism on Cu/Ag tandem catalysts surfaces is that *CO spills from Ag and subsequently undergoes symmetric dimerization to O*CCO in Cu. Considering that the strong Cu/Ag interfacial effect observed in this work, the coupling step is possible to be dominated by the Cu/Ag interface. The

symmetric coupling process from $^*\text{CO}$ - $^*\text{CO}$ to form O^*CCO on Cu (111) (1.11 eV) and Cu (111)/Ag (0.81 eV) surfaces requires a high uphill reaction energy (Fig. 3c). Moreover, on the Cu (100)/Ag surface (Fig. S32), the hydrogenation of $^*\text{CO}$ to $^*\text{CHO}$ (0.76 eV) is also energetically more favorable than the dimerization of $^*\text{CO}$ to O^*CCO (1.07 eV). The results indicate that C-C coupling via $^*\text{CO}$ dimerization is difficult on Cu surface and Cu/Ag interface, while $^*\text{CHO}$ formation is thermodynamically more favorable. In comparison with symmetric $^*\text{CO}$ - $^*\text{CO}$ coupling, which requires a high uphill reaction energy, the asymmetric coupling between $^*\text{CO}$ and $^*\text{CHO}$ intermediates on Cu (111)/Ag surface to form O^*CCHO is exergonic (Fig. 3c), while that on Cu (111) surface also has lower reaction energy (0.32 eV). Besides, the simultaneous hydrogenation of 2 $^*\text{CO}$ to form 2 $^*\text{CHO}$ requires a high reaction energy (1.19 eV in Fig. 3d), which limits the symmetric $^*\text{CHO}$ - $^*\text{CHO}$ coupling on Cu (111)/Ag surface. In addition, the energy barrier of the $^*\text{CHO}$ - $^*\text{CHO}$ coupling transition state (TS) is 0.61 eV (Fig. 3d and S33), which is much higher than that of the $^*\text{CO}$ - $^*\text{CHO}$ coupling (0.26 eV). Therefore, hydrogenation of $^*\text{CO}$ to form $^*\text{CHO}$ followed by coupling with $^*\text{CO}$ is the most thermodynamically favorable C-C coupling pathway.

As represented above, the appropriate atomic ratio and film thickness make the $\text{Cu}_{52}\text{Ag}_{48}$ sample with a thickness of 8 nm ($\text{Cu}_{52}\text{Ag}_{48}$ -8 nm) rich in Cu/Ag interfaces. Obviously, increasing the film thickness by maintaining a constant atomic ratio can decrease the proportion of Cu/Ag interface in the catalyst, and in turn, the bulk Cu properties may be enhanced. To further demonstrate the effect of the Cu/Ag interface on C_2H_4 generation, control catalysts named $\text{Cu}_{52}\text{Ag}_{48}$ -40 nm and $\text{Cu}_{52}\text{Ag}_{48}$ -100 nm were prepared with the film thicknesses of 40 nm and 100 nm (Table S5) by prolonging the sputtering time. The SEM images show that the size of nanoparticles on the GDE surface increases with increasing film thickness (Fig. S34). In the HRTEM image of $\text{Cu}_{52}\text{Ag}_{48}$ -40 nm (Fig. 4a), within the same area as Fig. 1d, only one Cu/Ag interface (indicated by a red dashed line) is observed. The selected area FFT images (Fig. 4b and c) confirm that areas (b) and (c) correspond to the Cu and Ag domains, respectively. Furthermore, the HRTEM image of $\text{Cu}_{52}\text{Ag}_{48}$ -100 nm shows that as the film thickness increases to 100 nm, the proportion of Cu/Ag interface decreases even further (Fig. S35). XPS spectra show that the surface Cu-Ag ratio is almost the same for both $\text{Cu}_{52}\text{Ag}_{48}$ -8 nm and $\text{Cu}_{52}\text{Ag}_{48}$ -40 nm (Table S6). However, the Ag 3d peaks of $\text{Cu}_{52}\text{Ag}_{48}$ -8 nm is shifted to high binding energy compared with $\text{Cu}_{52}\text{Ag}_{48}$ -40 nm (Fig. 4d). The LMM Auger and 2p peaks of Cu exhibit the shift consistent with that of Ag 3d spectra (Fig. 4e and S36). It indicates that there is stronger electron transfer between Cu and Ag in $\text{Cu}_{52}\text{Ag}_{48}$ -8 nm sample, further proving the presence of rich Cu/Ag interfaces in $\text{Cu}_{52}\text{Ag}_{48}$ -8 nm.

Based on these structural characterizations, the CO_2RR performance of $\text{Cu}_{52}\text{Ag}_{48}$ -40 nm and $\text{Cu}_{52}\text{Ag}_{48}$ -100 nm was further tested in a MEA system (Fig. 4f). At a current-density of 350 mA cm^{-2} , $\text{Cu}_{52}\text{Ag}_{48}$ -40 nm and $\text{Cu}_{52}\text{Ag}_{48}$ -100 nm exhibit the highest $\text{FE}_{\text{C}_2\text{H}_4}$ of 39.0% and 31.7%, respectively, which is much lower than the highest $\text{FE}_{\text{C}_2\text{H}_4}$ of 69.2% of $\text{Cu}_{52}\text{Ag}_{48}$ -8 nm. The ECSA (Fig. S37) test excludes the possibility that the increased performance is due to an increase in active area. In addition, as the thickness of the Cu/Ag catalysts increases (i.e. the Cu/Ag interface ratio decreased), the $\text{FE}_{\text{C}_2\text{H}_4}/\text{FE}_{\text{EtOH}}$ ratios decrease from 6.63 to 3.36 and 1.88 (Fig. 4g). This corroborates with the DFT results, indicating that the weak adsorption of H and the asymmetric $^*\text{CO}$ - $^*\text{CHO}$ coupling at the Cu/Ag interface promotes the formation of C_2H_4 at high current-density. As the interface ratio decreases, the properties of bulk Cu become more dominant, exhibiting $^*\text{CO}$ - $^*\text{CO}$ coupling and reducing the $\text{FE}_{\text{C}_2\text{H}_4}/\text{FE}_{\text{EtOH}}$ ratio. Moreover, the kinetic isotopic effect (KIE) of H/D (the ratio of C_2H_4 formation rates in H_2O and D_2O) are calculated to be close to 2:1 (Fig. 4h and S38), indicating that the dissociation of H_2O is involved in the rate-determining step, further proving the existence of hydrogenation of $^*\text{CO}$ to form $^*\text{CHO}$ followed by coupling with $^*\text{CO}$ in the Cu/Ag interface [6,21]. This is also consistent with the results of DFT calculations.

In-situ Raman spectroscopy tests were carried out at different potentials to reveal the reaction intermediates during CO_2RR , thus gaining a mechanistic insight into the catalytic differences between $\text{Cu}_{52}\text{Ag}_{48}$ -8 nm and $\text{Cu}_{52}\text{Ag}_{48}$ -40 nm. The Raman peaks of $\text{Cu}_{52}\text{Ag}_{48}$ -8 nm and $\text{Cu}_{52}\text{Ag}_{48}$ -40 nm (Fig. 4i and j) around 1324 cm^{-1} and 1600 cm^{-1} at 0 V are ascribed to the characteristic bands (D and G peak) of carbon paper [24]. As the potential increases, the enhanced Raman signals at 1324 cm^{-1} and 1600 cm^{-1} may correspond to HCO_3^- and H_2O [42]. In addition, the Raman peaks of two electrodes around 1067 cm^{-1} are ascribed to the CO_3^{2-} . The spectra collected from $\text{Cu}_{52}\text{Ag}_{48}$ -8 nm at -0.6 V exhibits a new peak in the $1900\text{--}2200 \text{ cm}^{-1}$ region (Fig. 4i). This peak corresponds to the stretching vibration of $^*\text{CO}$ on $\text{Cu}_{52}\text{Ag}_{48}$ -8 nm [12,43]. Based on the previous work, the spectra in the $\text{C}\equiv\text{O}$ stretched range can be convoluted as low-frequency band linear CO (LFB-CO) at $\sim 2060 \text{ cm}^{-1}$ and high-frequency band linear CO (HFB-CO) at $\sim 2095 \text{ cm}^{-1}$ [43,44]. The transformation of HFB-CO to LFB-CO suggests that $^*\text{CO}$ is heavily involved in chemical reactions and facilitates $^*\text{CO}$ - $^*\text{CO}$ coupling [43]. The peak ($\text{C}\equiv\text{O}$ stretching) of $\text{Cu}_{52}\text{Ag}_{48}$ -8 nm is centered at 2090 cm^{-1} (HFB-CO), and this peak shifts only slightly towards lower Raman shifts with increasing potential (from -0.6 V to -1.0 V). This suggests that $\text{Cu}_{52}\text{Ag}_{48}$ -8 nm with abundant Cu/Ag interface is not effective in triggering the $^*\text{CO}$ - $^*\text{CO}$ coupling. Notably, the spectra collected from $\text{Cu}_{52}\text{Ag}_{48}$ -8 nm at -0.7 V exhibits a new peak at 1674 cm^{-1} , which is ascribed to the asymmetric stretching vibration of $^*\text{CHO}$ intermediates [10,24]. DFT frequency calculations also support that the Raman band near 1674 cm^{-1} can be assigned as a $\text{C}=\text{O}$ stretching of $^*\text{CHO}$ species (Fig. S39). Moreover, in the low Raman shifts region, surface OH^- intermediates (690 cm^{-1}) on $\text{Cu}_{52}\text{Ag}_{48}$ -8 nm are also detected (Fig. S40) [12,24], further supporting the hydrogenation of $^*\text{CO}$ to $^*\text{CHO}$. The intensity of the $^*\text{CHO}$ intermediate decreases as the applied potential shifts negatively, and its peak position also shifts towards lower Raman shifts (from 1674 cm^{-1} to 1640 cm^{-1}). The redshift of band position with negative potentials is caused by the Stark effect [45], confirming that the $^*\text{CHO}$ is in-situ generated during CO_2RR . In addition, a peak attributed to the O^*CCHO intermediates formed after the coupling appeared at 1200 cm^{-1} in the Raman spectra of $\text{Cu}_{52}\text{Ag}_{48}$ -8 nm (-0.9 V), which can also be supported by DFT calculations (Fig. S39) [46,47]. The Raman bands of $^*\text{CHO}$ and O^*CCHO (hydrogen-containing intermediates) display nearly identical blue-shifts in the D_2O solvent-based electrolyte at -1.0 V , showing shifts of 107 cm^{-1} and 110 cm^{-1} , respectively (Fig. S41). This result suggests that the Raman bands around 1642 cm^{-1} and 1175 cm^{-1} are associated with hydrogen. Considering that the intensity of the $^*\text{CO}$ intermediate also decreases as the applied potential shifts negatively, it is speculated that a significant amount of asymmetric $^*\text{CO}$ - $^*\text{CHO}$ coupling occurs on the Cu/Ag interface at high potential. By contrast, the Raman spectra of $\text{Cu}_{52}\text{Ag}_{48}$ -40 nm does not detect the $^*\text{CHO}$ and O^*CCHO intermediates (Fig. 4j). The Raman spectra of $\text{Cu}_{52}\text{Ag}_{48}$ -40 nm (-0.4 V) exhibits a new peak at 1964 cm^{-1} , which associates with bridge-adsorbed CO [40]. The presence of $^*\text{CO}$ bridge, which requires at least two adjacent sites for its adsorption, is an indicator of enhanced Cu bulk properties [48]. Besides, the Raman peak for $\text{C}\equiv\text{O}$ stretching vibrations shifts from 2094 cm^{-1} to 2068 cm^{-1} as the potential increases from -0.7 V to -1.0 V . This potential-dependent behavior corresponds to the transformation of HFB-CO to LFB-CO, indicating that a significant amount of $^*\text{CO}$ intermediates on the $\text{Cu}_{52}\text{Ag}_{48}$ -40 nm surface participate in $^*\text{CO}$ - $^*\text{CO}$ coupling to form C_{2+} products.

Compared to the classical tandem effect observed in Cu/Ag catalysts, the novelty of our method is that the interfacial effect promotes the $^*\text{CHO}$ generation, while the tandem effect ensures the coverage of $^*\text{CO}$. As a result, asymmetric $^*\text{CO}$ - $^*\text{CHO}$ coupling reactions can occur, leading to high selectivity of C_2H_4 in CO_2RR under high current-density. The interfacial effect-induced $^*\text{CO}$ - $^*\text{CHO}$ coupling guides us to synthesize other useful catalysts for CO_2RR to C_2H_4 . Using other metal with weak H and O adsorption such as Zn or Au to replace Ag, we prepared $\text{Cu}_{49}\text{Zn}_{51}$ and $\text{Cu}_{64}\text{Au}_{36}$ catalysts (Experimental Methods and Table S7). The SEM

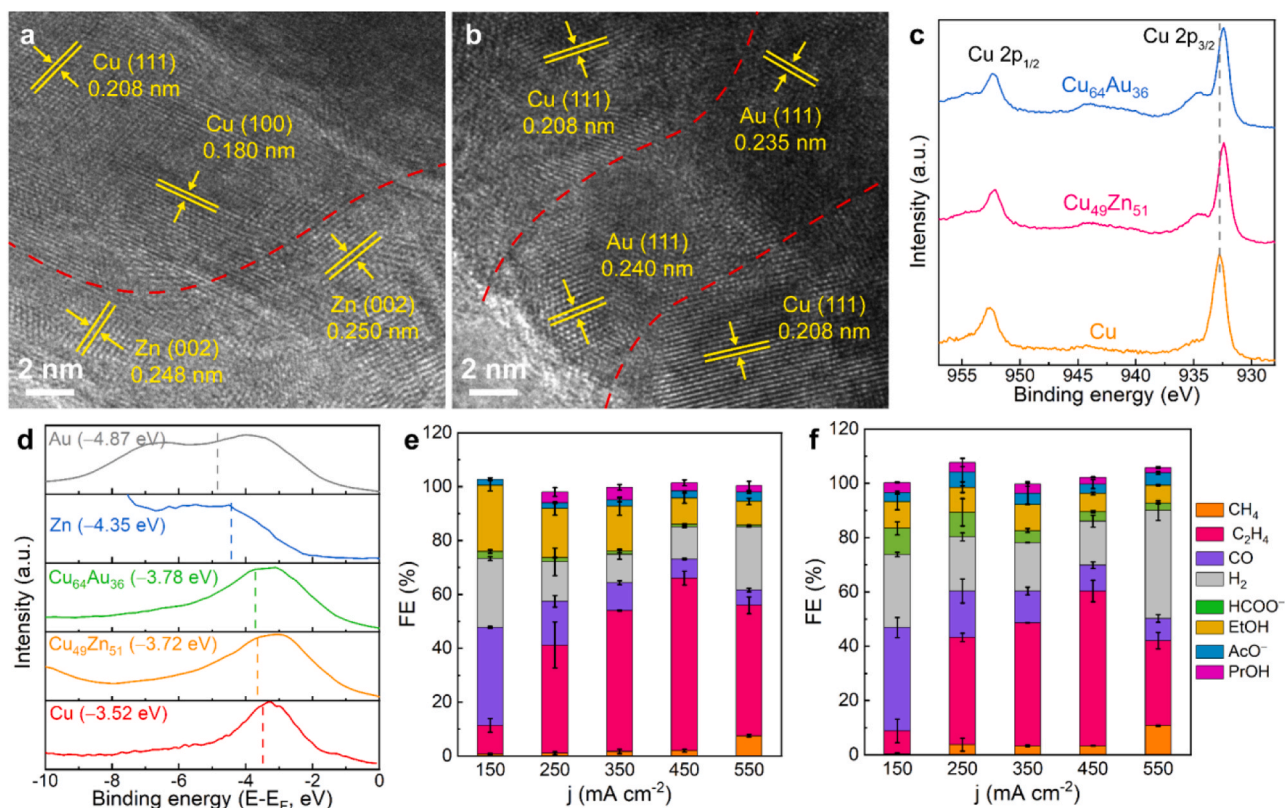


Fig. 5. HRTEM images of (a) Cu₄₉Zn₅₁ and (b) Cu₆₄Au₃₆. (c) Cu 2p XPS spectra of Cu, Cu₄₉Zn₅₁ and Cu₆₄Au₃₆. (d) Surface valence band spectra for Cu, Cu₄₉Zn₅₁, Cu₆₄Au₃₆, Zn and Au. FEs of major CO₂RR products obtained on (e) Cu₄₉Zn₅₁ and (f) Cu₆₄Au₃₆.

images and EDS elemental mapping in Fig. S42 show that the morphologies of Cu₄₉Zn₅₁ and Cu₆₄Au₃₆ are similar to that of the Cu₅₂Ag₄₈. In the HRTEM images of Cu₄₉Zn₅₁ and Cu₆₄Au₃₆ (Fig. 5a and b), Cu/Zn and Cu/Au domains are observed with clearly defined interfacial connections, which is highlighted by the red dashed line. The XPS spectra of Cu₄₉Zn₅₁ and Cu₆₄Au₃₆ further demonstrate the electron transfer at the Cu/Zn and Cu/Au interfaces (Fig. 5c and S43) and the gravity of the valence band spectra of Cu₄₉Zn₅₁ and Cu₆₄Au₃₆ shows a similar trend to that of Cu₅₂Ag₄₈ (Fig. 5d). As expected, both Cu₄₉Zn₅₁ and Cu₆₄Au₃₆ with abundant interfaces exhibit higher C₂H₄ selectivity than that of pure Cu (Fig. 5e and f). At a current-density of 450 mA cm⁻², the FE_{C₂H₄} of Cu₄₉Zn₅₁ and Cu₆₄Au₃₆ can reach 64.0% and 57.0%, respectively, indicating that the asymmetric *CO-*CHO coupling induced by the interface between Cu and metals with weak O and H adsorption capabilities is a general strategy to enhance the selectivity of C₂H₄ at high current-density.

4. Conclusions

In summary, the interfacial effect-induced *CO-*CHO coupling can promote the production of C₂H₄ at high current-density. The obtained Cu/Ag catalysts all demonstrate excellent CO₂RR performance toward C₂H₄, and Cu₅₂Ag₄₈ achieves a high FE_{C₂H₄} of 69.2% at 450 mA cm⁻² in the MEA system. DFT calculations indicate that the Cu/Ag interface reduces the energy barrier for *CO hydrogenation and promotes asymmetric *CO-*CHO coupling, which is critical for achieving high FE_{C₂H₄}. Moreover, in-situ Raman spectroscopy can detect both the *CHO intermediate and the asymmetric coupling intermediate O*CCHO. The interfacial effect-induced *CO-*CHO coupling can be extended to other metal with weak H and O adsorption, such as Cu/Zn and Cu/Au with FE_{C₂H₄} of 64.0% and 57.0% at 450 A cm⁻², respectively. This work provides new insights into the C-C coupling at the Cu/Ag interface, and the high activity of the Cu₅₂Ag₄₈ highlight its application potential in

realizing the industrial conversion of CO₂ to C₂H₄.

CRediT authorship contribution statement

Yong Zhang: Investigation, Methodology, Validation, Formal analysis, Data curation, Visualization, Writing – original draft. **FeiFei Chen:** Investigation, Formal analysis, Resources. **Xiaoya Hao:** Formal analysis, Investigation. **Yingda Liu:** Investigation, Formal analysis. **Wentao Wen:** Investigation, Formal analysis. **Xinghua Zhang:** Investigation, Formal analysis. **Zehao Zang:** Formal analysis, Resources. **Hong Dong:** Formal analysis, Resources. **Weihua Wang:** Formal analysis, Investigation. **Feng Lu:** Formal analysis, Investigation. **Zunming Lu:** Formal analysis, Investigation. **Hui Liu:** Formal analysis, Supervision. **Hui Liu:** Formal analysis, Writing – review & editing, Funding acquisition. **Feng Luo:** Formal analysis, Investigation. **Yahui Cheng:** Formal analysis, Project administration, Writing – review & editing, Conceptualization, Funding acquisition.

Declaration of Competing Interest

The authors declare that they have no known competing financial interests or personal relationships that could have appeared to influence the work reported in this paper.

Data Availability

Data will be made available on request.

Acknowledgments

This work was supported by the following grants: National Natural Science Foundation of China (No. 52071183, 51871122), Tianjin Research Innovation Project for Postgraduate Students (No.

2022SKY013).

Appendix A. Supporting information

Supplementary data associated with this article can be found in the online version at doi:10.1016/j.apcatb.2023.123666.

References

- [1] O.S. Bushuyev, P. De Luna, C.T. Dinh, L. Tao, G. Saur, J. van de Lagemaat, S. O. Kelley, E.H. Sargent, What should we make with CO₂ and how can we make it? *Joule* 2 (2018) 825–832.
- [2] Y.Y. Birdja, E. Pérez-Gallent, M.C. Figueiredo, A.J. Göttele, F. Calle-Vallejo, M.T. M. Koper, Advances and challenges in understanding the electrocatalytic conversion of carbon dioxide to fuels, *Nat. Energy* 4 (2019) 732–745.
- [3] W. Xi, P. Yang, M. Jiang, X. Wang, H. Zhou, J. Duan, M. Ratova, D. Wu, Electrochemical CO₂ reduction coupled with alternative oxidation reactions: Electrocatalysts, electrolytes, and electrolyzers, *Appl. Catal. B* 341 (2024), 123291.
- [4] M. Jouny, W. Luc, F. Jiao, General techno-economic analysis of CO₂ electrolysis systems, *Ind. Eng. Chem. Res.* 57 (2018) 2165–2177.
- [5] P. De Luna, R. Quintero-Bermudez, C.-T. Dinh, M.B. Ross, O.S. Bushuyev, P. Todorović, T. Regier, S.O. Kelley, P. Yang, E.H. Sargent, Catalyst electro-deposition controls morphology and oxidation state for selective carbon dioxide reduction, *Nat. Catal.* 1 (2018) 103–110.
- [6] C. Choi, S. Kwon, T. Cheng, M. Xu, P. Tieu, C. Lee, J. Cai, H.M. Lee, X. Pan, X. Duan, W.A. Goddard, Y. Huang, Highly active and stable stepped Cu surface for enhanced electrochemical CO₂ reduction to C₂H₄, *Nat. Catal.* 3 (2020) 804–812.
- [7] W. Liu, P. Zhai, A. Li, B. Wei, K. Si, Y. Wei, X. Wang, G. Zhu, Q. Chen, X. Gu, R. Zhang, W. Zhou, Y. Gong, Electrochemical CO₂ reduction to ethylene by ultrathin CuO nanoplate arrays, *Nat. Commun.* 13 (2022) 1877.
- [8] A. Vasileff, C. Xu, Y. Jiao, Y. Zheng, S.-Z. Qiao, Surface and interface engineering in copper-based bimetallic materials for selective CO₂ electroreduction, *Chem* 4 (2018) 1809–1831.
- [9] H. Xie, T. Zhang, R. Xie, Z. Hou, X. Ji, Y. Pang, S. Chen, M.M. Titirici, H. Weng, G. Chai, Facet engineering to regulate surface states of topological crystalline insulator bismuth rhombic dodecahedrons for highly energy efficient electrochemical CO₂ reduction, *Adv. Mater.* 33 (2021), e2008373.
- [10] B. Zhao, F. Chen, C. Cheng, L. Li, C. Liu, B. Zhang, C₆₀-stabilized Cu⁺ sites boost electrocatalytic reduction of CO₂ to C₂₊ products, *Adv. Energy Mater.* 13 (2023) 2204346.
- [11] T.-T. Zhuang, Z.-Q. Liang, A. Seifitokaldani, Y. Li, P. De Luna, T. Burdyny, F. Che, F. Meng, Y. Min, R. Quintero-Bermudez, C.T. Dinh, Y. Pang, M. Zhong, B. Zhang, J. Li, P.-N. Chen, X.-L. Zheng, H. Liang, W.-N. Ge, B.-J. Ye, D. Sinton, S.-H. Yu, E. H. Sargent, Steering post-C-C coupling selectivity enables high efficiency electroreduction of carbon dioxide to multi-carbon alcohols, *Nat. Catal.* 1 (2018) 421–428.
- [12] J. Gao, H. Zhang, X. Guo, J. Luo, S.M. Zakeeruddin, D. Ren, M. Gratzel, Selective C-C coupling in carbon dioxide electroreduction via efficient spillover of intermediates as supported by operando raman spectroscopy, *J. Am. Chem. Soc.* 141 (2019) 18704–18714.
- [13] Y. Ma, J. Yu, M. Sun, B. Chen, X. Zhou, C. Ye, Z. Guan, W. Guo, G. Wang, S. Lu, D. Xia, Y. Wang, Z. He, L. Zheng, Q. Yun, L. Wang, J. Zhou, P. Lu, J. Yin, Y. Zhai, Z. Luo, L. Zhai, L. Liao, Z. Zhu, R. Ye, Y. Chen, Y. Lu, S. Xi, B. Huang, C.S. Lee, Z. Fan, Confined growth of silver-copper janus nanostructures with {100} facets for highly selective tandem electrocatalytic carbon dioxide reduction, *Adv. Mater.* 34 (2022), e2110607.
- [14] T.H.M. Pham, J. Zhang, M. Li, T.H. Shen, Y. Ko, V. Tileli, W. Luo, A. Züttel, enhanced electrocatalytic CO₂ reduction to C₂₊ products by adjusting the local reaction environment with polymer binders, *Adv. Energy Mater.* 12 (2022) 2103663.
- [15] A.J. Garza, A.T. Bell, M. Head-Gordon, Mechanism of CO₂ reduction at copper surfaces: pathways to C₂ products, *ACS Catal.* 8 (2018) 1490–1499.
- [16] J.D. Goodpaster, A.T. Bell, M. Head-Gordon, Identification of possible pathways for C-C bond formation during electrochemical reduction of CO₂: new theoretical insights from an improved electrochemical model, *J. Phys. Chem. Lett.* 7 (2016) 1471–1477.
- [17] J.A. Gauthier, Z. Lin, M. Head-Gordon, A.T. Bell, Pathways for the formation of C₂₊ products under alkaline conditions during the electrochemical reduction of CO₂, *ACS Energy Lett.* 7 (2022) 1679–1686.
- [18] T. Cheng, H. Xiao, W.A. Goddard 3rd, Full atomistic reaction mechanism with kinetics for CO reduction on Cu(100) from ab initio molecular dynamics free-energy calculations at 298 K, *Proc. Natl. Acad. Sci. USA* 114 (2017) 1795–1800.
- [19] C. Chen, S. Yu, Y. Yang, S. Louisiana, I. Roh, J. Jin, S. Chen, P.-C. Chen, Y. Shan, P. Yang, Exploration of the bio-analogous asymmetric C-C coupling mechanism in tandem CO₂ electroreduction, *Nat. Catal.* 5 (2022) 878–887.
- [20] W. Ma, S. Xie, T. Liu, Q. Fan, J. Ye, F. Sun, Z. Jiang, Q. Zhang, J. Cheng, Y. Wang, Electrocatalytic reduction of CO₂ to ethylene and ethanol through hydrogen-assisted C-C coupling over fluorine-modified copper, *Nat. Catal.* 3 (2020) 478–487.
- [21] Y. Liang, J. Zhao, Y. Yang, S.F. Hung, J. Li, S. Zhang, Y. Zhao, A. Zhang, C. Wang, D. Appadoo, L. Zhang, Z. Geng, F. Li, J. Zeng, Stabilizing copper sites in coordination polymers toward efficient electrochemical C-C coupling, *Nat. Commun.* 14 (2023) 474.
- [22] M. Luo, Z. Wang, Y.C. Li, J. Li, F. Li, Y. Lum, D.H. Nam, B. Chen, J. Wicks, A. Xu, T. Zhuang, W.R. Leow, X. Wang, C.T. Dinh, Y. Wang, Y. Wang, D. Sinton, E. H. Sargent, Hydroxide promotes carbon dioxide electroreduction to ethanol on copper via tuning of adsorbed hydrogen, *Nat. Commun.* 10 (2019) 5814.
- [23] T. Zhang, B. Yuan, W. Wang, J. He, X. Xiang, Tailoring *H intermediate coverage on the CuAl₂O₄/CuO catalyst for enhanced electrocatalytic CO₂ reduction to ethanol, *Angew. Chem. Int. Ed.* 62 (2023), e202302096.
- [24] X. Yan, M. Zhang, Y. Chen, Y. Wu, R. Wu, Q. Wan, C. Liu, T. Zheng, R. Feng, J. Zhang, C. Chen, C. Xia, Q. Zhu, X. Sun, Q. Qian, B. Han, Synergy of Cu/C₃N₄ interface and Cu nanoparticles dual catalytic regions in electrolysis of CO to acetic acid, *Angew. Chem. Int. Ed.* 62 (2023), e202301507.
- [25] H. Xiao, T. Cheng, W.A. Goddard 3rd, Atomistic mechanisms underlying selectivities in C₁ and C₂ products from electrochemical reduction of CO on Cu (111), *J. Am. Chem. Soc.* 139 (2017) 130–136.
- [26] Y.C. Li, Z. Wang, T. Yuan, D.H. Nam, M. Luo, J. Wicks, B. Chen, J. Li, F. Li, F.P. G. de Arquer, Y. Wang, C.T. Dinh, O. Voznyy, D. Sinton, E.H. Sargent, Binding site diversity promotes CO₂ electroreduction to ethanol, *J. Am. Chem. Soc.* 141 (2019) 8584–8591.
- [27] Z. Cai, N. Cao, F. Zhang, X. Lv, K. Wang, Y. He, Y. Shi, H. Bin Wu, P. Xie, Hierarchical Ag-Cu interfaces promote C-C coupling in tandem CO₂ electroreduction, *Appl. Catal. B* 325 (2023), 122310.
- [28] T. Zhang, J.C. Bui, Z. Li, A.T. Bell, A.Z. Weber, J. Wu, Highly selective and productive reduction of carbon dioxide to multicarbon products via in situ CO management using segmented tandem electrodes, *Nat. Catal.* 5 (2022) 202–211.
- [29] H. Li, P. Yu, R. Lei, F. Yang, P. Wen, X. Ma, G. Zeng, J. Guo, F.M. Toma, Y. Qiu, S. M. Geyer, X. Wang, T. Cheng, W.S. Drisdell, Facet-selective deposition of ultrathin Al₂O₃ on copper nanocrystals for highly stable CO₂ electroreduction to ethylene, *Angew. Chem. Int. Ed.* 60 (2021) 24838–24843.
- [30] X. Feng, K. Jiang, S. Fan, M.W. Kanan, Grain-boundary-dependent CO₂ electroreduction activity, *J. Am. Chem. Soc.* 137 (2015) 4606–4609.
- [31] D. Kim, J. Resasco, Y. Yu, A.M. Asiri, P. Yang, Synergistic geometric and electronic effects for electrochemical reduction of carbon dioxide using gold-copper bimetallic nanoparticles, *Nat. Commun.* 5 (2014) 4948.
- [32] J.K. Nørskov, T. Bligaard, J. Rossmeisl, C.H. Christensen, Towards the computational design of solid catalysts, *Nat. Chem.* 1 (2009) 37–46.
- [33] C.-T. Dinh, T. Burdyny, M.G. Kibria, A. Seifitokaldani, C.M. Gabardo, F.P. García de Arquer, A. Kiani, J.P. Edwards, P. De Luna, O.S. Bushuyev, C. Zou, R. Quintero-Bermudez, Y. Pang, D. Sinton, E.H. Sargent, CO₂ electroreduction to ethylene via hydroxide-mediated copper catalysis at an abrupt interface, *Science* 360 (2018) 783–787.
- [34] J. Gu, S. Liu, W. Ni, W. Ren, S. Haussener, X. Hu, Modulating electric field distribution by alkali cations for CO₂ electroreduction in strongly acidic medium, *Nat. Catal.* 5 (2022) 268–276.
- [35] Y. Xie, P. Ou, X. Wang, Z. Xu, Y.C. Li, Z. Wang, J.E. Huang, J. Wicks, C. McCallum, N. Wang, Y. Wang, T. Chen, B.T.W. Lo, D. Sinton, J.C. Yu, Y. Wang, E.H. Sargent, High carbon utilization in CO₂ reduction to multi-carbon products in acidic media, *Nat. Catal.* 5 (2022) 564–570.
- [36] B. Pan, J. Fan, J. Zhang, Y. Luo, C. Shen, C. Wang, Y. Wang, Y. Li, Close to 90% Single-pass conversion efficiency for CO₂ electroreduction in an acid-fed membrane electrode assembly, *ACS Energy Lett.* 7 (2022) 4224–4231.
- [37] L. Li, Z. Liu, X. Yu, M. Zhong, Achieving high single-pass carbon conversion efficiencies in durable CO₂ electroreduction in strong acids via electrode structure engineering, *Angew. Chem. Int. Ed.* 62 (2023), e202300226.
- [38] Z. Gu, H. Shen, Z. Chen, Y. Yang, C. Yang, Y. Ji, Y. Wang, C. Zhu, J. Liu, J. Li, T.-K. Sham, X. Xu, G. Zheng, Efficient electrocatalytic CO₂ reduction to C₂₊ alcohols at defect-site-rich Cu surface, *Joule* 5 (2021) 429–440.
- [39] S. Ma, M. Sadakiyo, M. Heima, R. Luo, R.T. Haasch, J.I. Gold, M. Yamauchi, P. J. Kenis, Electroreduction of carbon dioxide to hydrocarbons using bimetallic Cu-Pd catalysts with different mixing patterns, *J. Am. Chem. Soc.* 139 (2017) 47–50.
- [40] P. Wang, H. Yang, C. Tang, Y. Wu, Y. Zheng, T. Cheng, K. Davey, X. Huang, S. Z. Qiao, Boosting electrocatalytic CO₂-to-ethanol production via asymmetric C-C coupling, *Nat. Commun.* 13 (2022) 3754.
- [41] S. Kuang, Y. Su, M. Li, H. Liu, H. Chuai, X. Chen, E.J.M. Hensen, T.J. Meyer, S. Zhang, X. Ma, Asymmetrical electrohydrogenation of CO₂ to ethanol with copper-gold heterojunctions, *Proc. Natl. Acad. Sci. USA* 120 (2023), e2214175120.
- [42] X. Chen, J. Chen, N.M. Alghoraibi, D.A. Henckel, R. Zhang, U.O. Nwabara, K. E. Madsen, P.J.A. Kenis, S.C. Zimmerman, A.A. Gewirth, Electrochemical CO₂-to-ethylene conversion on polyamine-incorporated Cu electrodes, *Nat. Catal.* 4 (2021) 20–27.
- [43] H. An, L. Wu, L.D.B. Mandemaker, S. Yang, J. de Ruiter, J.H.J. Wijten, J.C. L. Janssens, T. Hartman, W. van der Stam, B.M. Weckhuysen, Sub-second time-resolved surface-enhanced raman spectroscopy reveals dynamic CO intermediates during electrochemical CO₂ reduction on copper, *Angew. Chem. Int. Ed.* 60 (2021) 16576–16584.
- [44] C.M. Gunathunge, J. Li, X. Li, J.J. Hong, M.M. Waegle, revealing the predominant surface facets of rough Cu electrodes under electrochemical conditions, *ACS Catal.* 10 (2020) 6908–6923.
- [45] I.V. Chernyshova, P. Somasundaran, S. Ponnurangam, On the origin of the elusive first intermediate of CO₂ electroreduction, *Proc. Natl. Acad. Sci. USA* 115 (2018) E9261–E9270.

- [46] E. Perez-Gallent, M.C. Figueiredo, F. Calle-Vallejo, M.T. Koper, Spectroscopic observation of a hydrogenated CO dimer intermediate during CO reduction on Cu (100) electrodes, *Angew. Chem. Int. Ed.* 56 (2017) 3621–3624.
- [47] Y. Kim, S. Park, S.-J. Shin, W. Choi, B.K. Min, H. Kim, W. Kim, Y.J. Hwang, Time-resolved observation of C–C coupling intermediates on Cu electrodes for selective electrochemical CO₂ reduction, *Energy Environ. Sci.* 13 (2020) 4301–4311.
- [48] H. Shen, Y. Wang, T. Chakraborty, G. Zhou, C. Wang, X. Fu, Y. Wang, J. Zhang, C. Li, F. Xu, L. Cao, T. Mueller, C. Wang, Asymmetrical C–C coupling for electroreduction of CO on bimetallic Cu–Pd catalysts, *ACS Catal.* 12 (2022) 5275–5283.